Available online at www.sciencedirect.com
ScienceDirect
Journal of the European Ceramic Society 28 (2008) 329–344
www.elsevier.com/locate/jeurceramsoc

Structure and properties of mullite—A review

H. Schneider [a,*], J. Schreuer [b], B. Hildmann [a]

[a] *Institute of Materials Research, German Aerospace Center (DLR), D-51140 Köln, Germany*
[b] *Institute of Geology, Mineralogy and Geophysics, Ruhr-University, Bochum 44801, Germany*

Available online 2 May 2007

Abstract

Mullite has achieved outstanding importance as a material for both traditional and advanced ceramics because of its favourable thermal and mechanical properties. Mullite displays various Al to Si ratios referring to the solid solution $Al_{4+2x}Si_{2-2x}O_{10-x}$, with x ranging between about 0.2 and 0.9 (about 55 to 90 mol% Al_2O_3). Depending on the synthesis temperature and atmosphere mullite is able to incorporate a number of transition metal cations and other foreign atoms. The crystal structure of mullite is closely related to that of sillimanite, which is characterized by chains of edge-connected AlO_6 octahedra running parallel to the crystallographic c-axis. These very stiff chains are cross-linked by tetrahedral chains consisting of $(Al,Si)O_4$ tetrahedra. In more detail: Parallel to **a** the tetrahedra are linked to the relatively short more stiff Al–O(A, B) bonds, whereas parallel **b** they are linked parallel to the relatively long more compliant Al–O(D) bonds. In mullite some of the oxygen atoms bridging the tetrahedra are removed for charge compensation. This gives rise to the formation of oxygen vacancies and of T_3O groups (so-called tetrahedral triclusters).

The anisotropy of the bonding system of mullite has a major influence on the anisotropy of its physical properties. For example:

- the highest longitudinal elastic stiffness is observed parallel **c**, but lower ones parallel **a** and especially parallel **b**,
- the maximum of the thermal conductivity occurs parallel **c**, but maller ones parallel **a** and especially parallel **b**,
- large thermal expansion especially parallel **b**,
- fastest crystal growth and highest corrosion parallel **c**.

Heat capacity and thermal expansion measurements of mullite display reversible anomalies in the temperature range between about 1000 and 1200 °C. It is believed that tetrahedral cations, bridging O atoms, and O vacancies undergo dynamical site exchange processes at high temperatures. At lower temperatures the dynamic disorder may transform to a static one. Diffraction experiments revealed that also partially ordered states may exist.

Keywords: Mullite; Chemical properties; Mechanical properties; Thermal properties; Crystal structure

1. Introduction

Due to its high temperature but low pressure formation conditions, mullite occurs very rarely in nature. It has been found at the contact of superheated magma intrusions with Al_2O_3-rich sediments, as on the Island of Mull (Scotland), where the name mullite comes from. Mullite has also been described in high temperature metamorphosed rocks of the sanidinite facies[1] and in hornfelses (porcellanite), e.g., at the contact of bauxites with olivine dolerite intrusions. Special and rare occurrences of mullite are in alumino silicate lechatelerite glasses produced by lightening impact in sandstones,[2] and in small druses of volcanic rocks (e.g., in the Eifel mountain, Western Germany), where it probably grew under moderate hydrothermal conditions (Fig. 1(a) and (b)). In spite of its rare occurrence in natural rocks mullite is perhaps one of the most important phases in both traditional and advanced ceramics. The importance of mullite and mullite ceramics is documented by the big number of publications, which appeared in recent years (Fig. 2). The outstanding scientific and technical importance of mullite can be explained by

- Its high thermal stability and the favorable properties like low thermal expansion and conductivity, high creep resistance and corrosion stability together with suitable strength and fracture toughness (Table 1).

* Corresponding author. Present address: Institute of Crystallography, University of Köln, 50674 Köln, Germany. Tel.: +49 221 4702532; fax: +49 221 4704963.
E-mail address: Hartmut.Schneider@uni-koeln.de (H. Schneider).

0955-2219/$ – see front matter © 2007 Elsevier Ltd. All rights reserved.
doi:10.1016/j.jeurceramsoc.2007.03.017

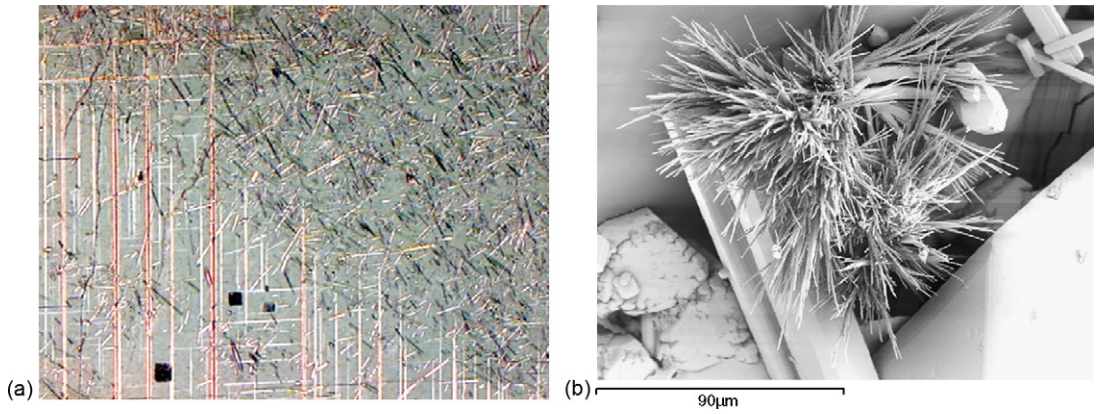

Fig. 1. Natural mullite. (a) Thin section micrograph of the lava of the Ben More volcano (Island of Mull, Scotland), where mullite has been described for the first time in nature. Note the occurrence of tiny mullite needles, overgrown by plagioclase. (b) Scanning electron micrograph of mullite needles grown hydrothermally in small druses of volcanic rocks of the Eifel mountain (Germany, Courtesy B. Ternes).

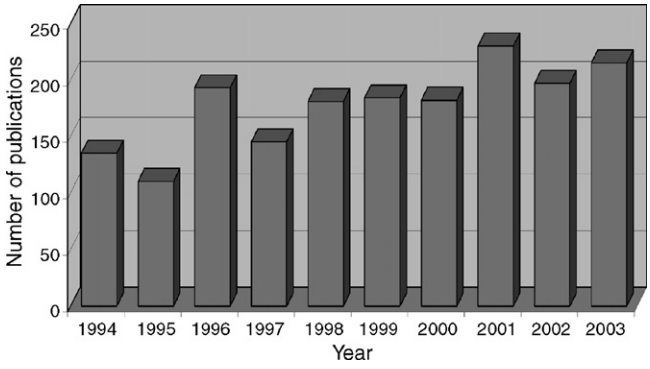

Fig. 2. Number of publications dealing primarily with mullite and mullite ceramics, and which appeared between 1994 and 2003 (from Web of Science, 2005).

- The fact that the starting materials (e.g., α-alumina plus silica, alumino silicates of the composition Al_2SiO_5, i.e., sillimanite, andalusite and kyanite, refractory-grade bauxite, Al_2O_3-rich sheet silicates and clays) are available in big quantities on earth. Thereby kaolinite and other clay-based materials achieved high importance, since they allow multiple shaping procedures of components and structures in the green state.
- Its ability to form mixed crystals in a wide Al_2O_3/SiO_2 range and to incorporate a large variety of foreign cations into the structure.
- The fact that the structural principles of mullite senso stricto can be extended to a large number of phases belonging to the family of mullite-type structures.

Mullite and mullite ceramics display a large variety of appearances, reaching from Czochralski-grown single crystals to polycrystalline and polyphase ceramics, and from very large refractory products to very tiny engineering components of high purity and homogeneity (Fig. 3).

Basically three types of polycrystalline mullite ceramics may be distinguished: monolithic mullite ceramics, mullite coatings and mullite matrix composites.

1.1. Monolithic mullite ceramics

Monolithic mullite ceramics have widely been used for both traditional and advanced applications. Important materials are tableware, porcelain, construction and engineering ceramics, refractories, kiln furnitures, creep resistant materials, substrates for catalytic convertors, electronic devices, and

Table 1
Thermo-mechanical properties of mullite ceramics and other advanced oxide ceramics

Compound	Tieillite	Cordierite	Spinel	α-Alumina	Zirconia	Mullite
Composition	$Al_2O_3{\cdot}TiO_2$	$2MgO{\cdot}2Al_2O_3{\cdot}5SiO_2$	$MgO{\cdot}Al_2O_3$	Al_2O_3	ZrO_2	$3Al_2O_3{\cdot}2SiO_2$
Melting point (°C)	1860	1465	2135	2050	2600	≈1830
Density ($g\,cm^{-3}$)	3.68	2.2	3.56	3.96	5.60	≈3.2
Linear thermal expansion ($\times 10^{-6}\,°C^{-1}$)						
20–1400 °C	≈1	≈0	9	8	10	≈4.5
Thermal conductivity ($kcal\,m^{-1}\,h^{-1}\,°C^{-1}$)						
20 °C	1.5–2	≈10–15	13	26	1.5	6
1400 °C	2.5	–	4	4	2	3
Strength (MPa)	30	120	180	500	200	≈200
Fracture toughness K_{Ic} ($MPa\,m^{0.5}$)	–	≈1.5	–	≈4.5	≈2.4	≈2.5

If not indicated otherwise, values are given at room temperature.

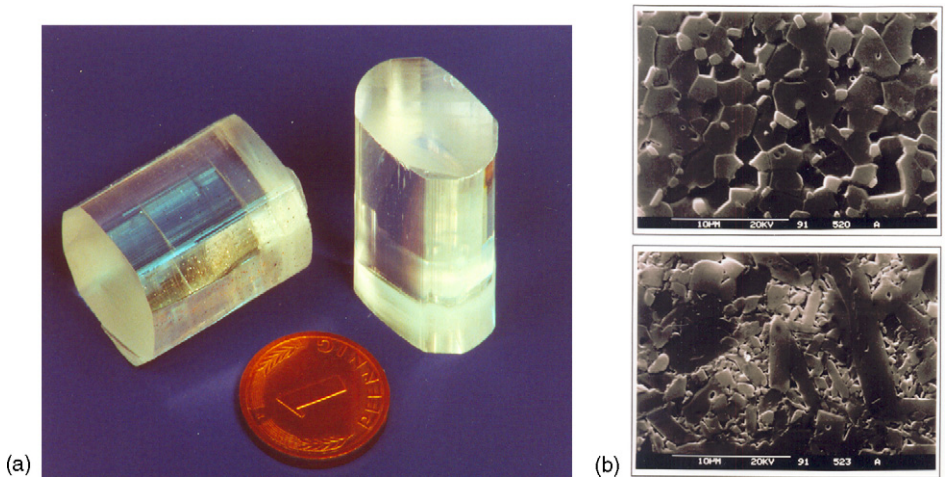

Fig. 3. Technical-grade mullites. (a) Czochralski-grown mullite single crystals of 2/1-composition (≈77 wt.% Al_2O_3). (b) Microstructures of fully dense polycrystalline mullite ceramics with different bulk Al_2O_3 compositions (top: ≈72 wt.%, bottom: ≈78 wt.%), produced from co-precipitated precursors via sintering and hot isostatic pressing. Note the different distribution of mullite (dark) and α-alumina grains (light).

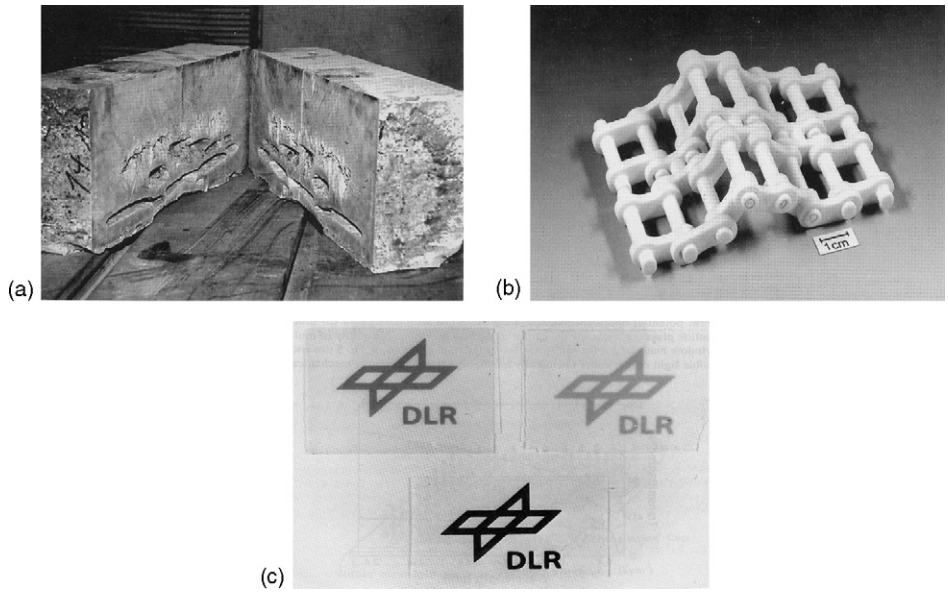

Fig. 4. Monolithic mullite ceramics. Examples for technical applications. (a) Fused-mullite refractory bricks. These materials are highly corrosion resistant and are frequently used in glass melting tanks. (b) Sinter-mullite-based conveyor belt for continuous charging of annealing furnaces. Because of their good thermal shock resistance such structures have been used in furnaces for the temperature treatment of electronic packaging materials. (c) Optically translucent mullite. Such compounds have been used for high-temperature furnace windows.

other advanced ceramics (e.g., optically translucent ceramics for high-temperature furnace windows, Fig. 4).

1.2. Mullite coatings

Many metals and ceramics are susceptible to degradation when exposed to oxidizing, reducing or to other harsh chemical environments at high temperature. A suitable way to overcome these problems is to protect such materials by surface coatings with compounds being stable under the required conditions (so-called environmental barrier coatings, EBCs). Mullite EBCs have successfully been applied for oxide- or nonoxide-based ceramic structures for multiple uses, e.g., for furnace tubes and for the heat shield of space re-entry vehicles (Fig. 5).

1.3. Mullite matrix composites

This material group includes composites with mullite matrices and mullite fibers. The main aim of research and development in the field of mullite composites is the reduction of the inherent brittleness of the systems by improvement of their toughness. Although there was much effort in the last two decades to improve the thermo-mechanical behavior of mullite matrices by platelet and particle reinforcement (especially silicon carbide, zirconia, α-alumina) a break through has not been achieved. In recent years major activities have been focussed on continuous fiber-reinforced mullite matrix composites, especially using α-alumina and mullite fibers. Important application fields of such composites are components and structures for gas

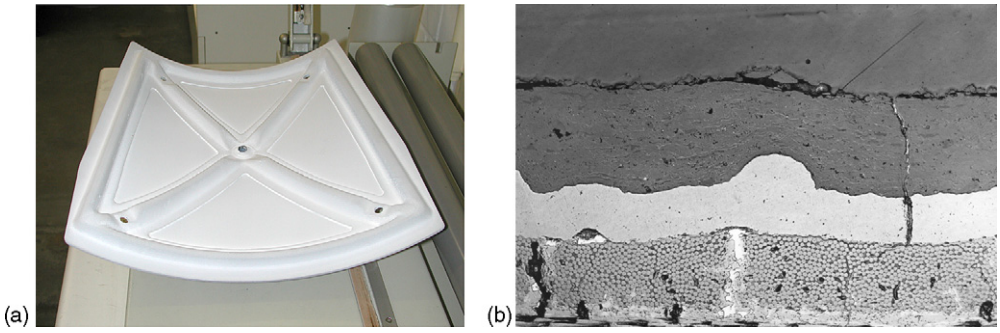

Fig. 5. Mullite coatings. Examples of technical applications. (a) Panel for a re-entry space vehicle (mullite-coated C/C–SiC composite). (b) Microstructure of a vacuum plasma mullite-coated C/C–SiC composite. Note the occurrence of the SiC bond coat between C/C–SiC substrate and mullite coating.

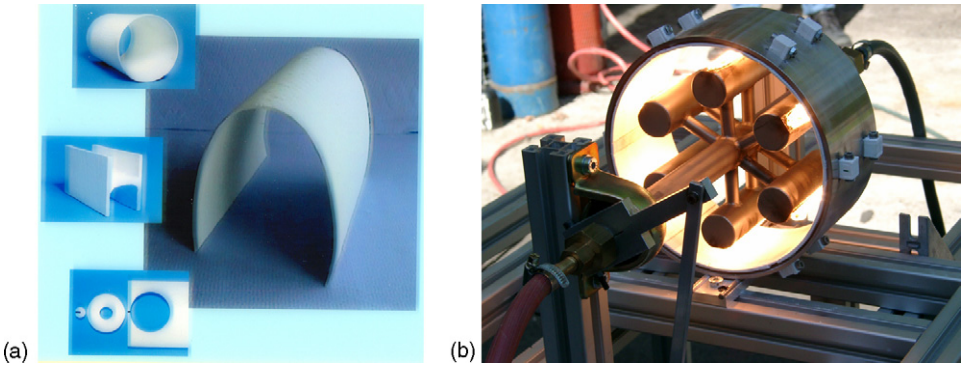

Fig. 6. Mullite matrix composites. Examples of technical applications. (a) Components and structures made of mullite fiber-reinforced mullite matrix composites (WHIPOX, *w*ound *hi*ghly *p*orous *ox*ide matrix composite, registered trade mark) for various technical uses. (b) Segmented combuster tiles made of WHIPOX for the use as thermal protection systems in combustors of stationary and aircraft gas turbine engines (DLR demonstrator).

turbine engines (liners, thermal protection shingles for combustors, exhaust cones), high duty kiln furnitures, burner tubes, and heat shields for re-entry space vehicles (Fig. 6).

2. Crystal chemistry of mullite

This chapter deals with the principles of the crystal structure of mullite senso stricto with alumino silicate composition, and with the foreign cation incorporation into mullite. Other members of the family of mullite-type structures and the relationships between them are not described here. The paper will also not deal with the non-crystalline mullite gels and glasses or with other mullite precursors. For getting more information in these fields the reader is referred to the review articles of Fischer and Schneider[3] and Schmücker and Schneider.[4]

2.1. The crystal structure of mullite

Mullite senso stricto displays variable aluminum to silicon ratios referring to the solid solution series $Al_{4+2x}Si_{2-2x}O_{10-x}$, with x ranging between about 0.2 and 0.9 (corresponding to about 55–90 mol% Al_2O_3[5]). Various types of mullites, depending on their synthesis procedures have been described as being relevant for ceramics:

- Sinter-mullites, produced by heat treatment of the starting materials, essentially via solid-state reactions. These mullites tend to have "stoichiometric", i.e., 3/2-composition ($3Al_2O_3{\cdot}2SiO_2$, i.e., ≈72 wt.% Al_2O_3, $x = 0.25$, Table 2).
- Fused-mullites, produced by crystallizing of alumino silicate melts. These mullites tend to be Al_2O_3-rich with approxi-

Table 2
Structural data of 3/2- and 2/1-mullites

Composition x	Name	Space group	Lattice parameters				Reference
			a (Å)	b (Å)	c (Å)	V (Å^3)	
0	Sillimanite	*Pbnm*	7.486	7.675	5.775	331.8	Burnham[6]
0.25	3/2-Mullite	*Pbam*	7.553	7.686	2.8864	167.6	Saalfeld and Guse[10]
0.40	2/1-Mullite	*Pbam*	7.588	7.688	2.8895	168.6	Angel et al.[9]

The x-value refers to the general composition of mullite $Al_{4+2x}Si_{2-2x}O_{10-x}$, x giving the number of oxygen vacancies per unit cell.

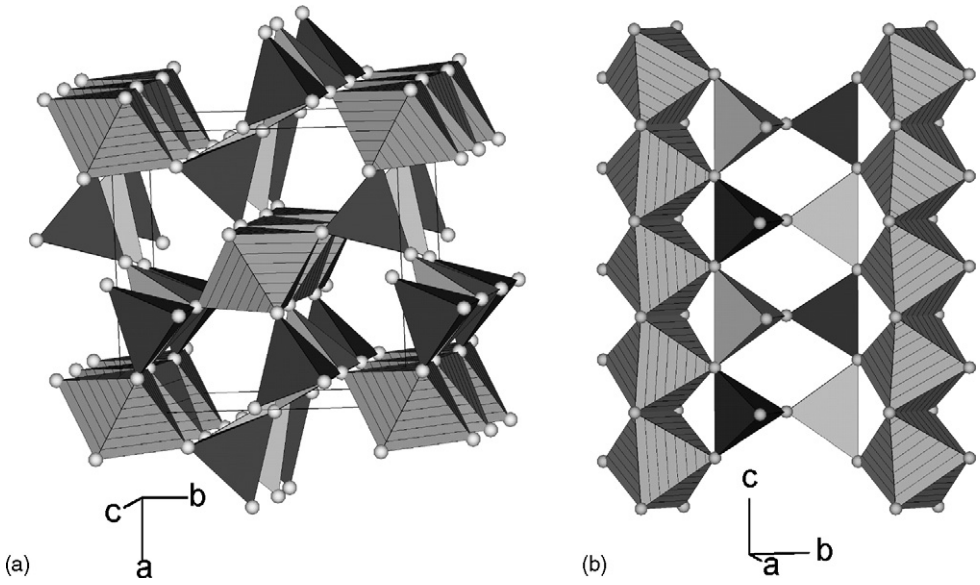

Fig. 7. Crystal structure of sillimanite in projections down (a) the *c*-axis, and (b) the *a*-axis (from Fischer and Schneider).[3] Sillimanite provides a simple model to explain structural relationships in mullite.

mate 2/1-composition ($2Al_2O_3{\cdot}SiO_2$, i.e., ≈78 wt.% Al_2O_3, $x = 0.40$, Table 2).

- Chemical-mullites, produced by heat treatment of organic or inorganic precursors. The composition of such mullites strongly depends on the starting materials and the temperature treatment. Extremely Al_2O_3-rich compounds (>90 wt.% Al_2O_3, $x > 0.80$) have been identified at synthesis temperatures <1000 °C.

The average structure of mullite can be derived from the closely related but structurally more simple sillimanite (composition: Al_2SiO_5, $x = 0.00$). In sillimanite, like in other mullite-type structures, edge-connected AlO_6 octahedral chains run parallel to the crystallographic *c*-axis.[6–8] In sillimanite these octahedral chains are cross-linked by double chains with alternating AlO_4 and SiO_4 tetrahedra (Fig. 7). Formally mullite can be derived from sillimanite by a coupled substitution, according to

$$2Si^{4+} + O^{2-} \rightarrow 2Al^{3+} + \square$$

$\square$ = oxygen vacancy.

This reaction involves removal of oxygen atoms from the structure leading to oxygen vacancies and to a rearrangement and disordering of tetrahedral cations. Structure refinements indicate that the oxygen atoms bridging two polyhedra in the tetrahedral double chain in sillimanite (so-called O(C) atoms, see Fig. 8) are removed in mullite. Simultaneously the two tetrahedral cations originally linked to this O(C) site are displaced to a position designated as T^* (big arrows in Fig. 8), and O(C) becomes threefold coordinated by cations forming T_3O groups (so-called triclusters). It has generally been accepted that the triclusters are preferably occupied by Al. The number of oxygen vacancies corresponds directly to the *x*-value of the mullite mixed crystal series $Al_{4+2x}Si_{2-2x}O_{10-x}$. The *c* lattice constant of mullite is halfed with respect to that of sillimanite, because Al and Si atoms are randomly distributed over the tetrahedral cation sites in mullite. Structural data including space group and lattice constants obtained for 3/2-mullite ($x = 0.25$) and 2/1-mullite ($x = 0.40$), respectively, are summarized in Table 2 in comparison to those of sillimanite.[3,6–10]

Due to the various possible arrangements of oxygen vacancies and of tetrahedrally bound Al and Si atoms the local structure of mullite can slightly deviate from the average situation. Information on the local (real) structure has been obtained from the additional scattered diffuse intensities and superstructure reflections occurring in single crystal diffraction patterns. Superstructure reflections are attributed to a partial ordering of oxygen vacancies, and of Al and Si atoms over the tetrahedral sites.[11] Further information on the degree of the tetrahedral Al to Si ordering in mullite has been derived from ^{29}Si nuclear magnetic resonance (NMR) spectroscopy.[12] In contrast to sillimanite, which exhibits only one strong ^{29}Si NMR signal near −88 ppm, mullite displays two more though weak signals near −92 and −95 ppm. The intense signal near −88 ppm is assigned to three AlO_4 tetrahedra in the next nearest environment of a SiO_4 tetrahedron. Since it is present in the ^{29}Si NMR spectra of sillimanite and mullite it may reflect a sillimanite-type local order in the tetrahedra. The NMR peaks near −92 and −95 ppm were assigned to two AlO_4 and one SiO_4 tetrahedra, and to one AlO_4 and two SiO_4 tetrahedra, respectively, being next nearest neighbors of SiO_4.[12] The comparison of measured with simulated ^{29}Si NMR intensities yields a moderate degree of Al and Si ordering in the tetrahedra of mullite. According to in situ high-temperature X-ray diffraction studies of Paulmann[13] the ordering scheme of oxygen vacancies and of tetrahedral Al and Si is very stable and persists up to the melting point of mullite.

Burnham[14] mentioned that the mullite structure theoretically fits all compositions between (disordered) sillimanite ($x = 0.00$) and aluminum oxide with mullite structure (ι-alumina, $x = 1.00$), and that there is no obvious reason why the composition should be restricted to 3/2-mullite ($x = 0.25$) or 2/1-mullite ($x = 0.40$),

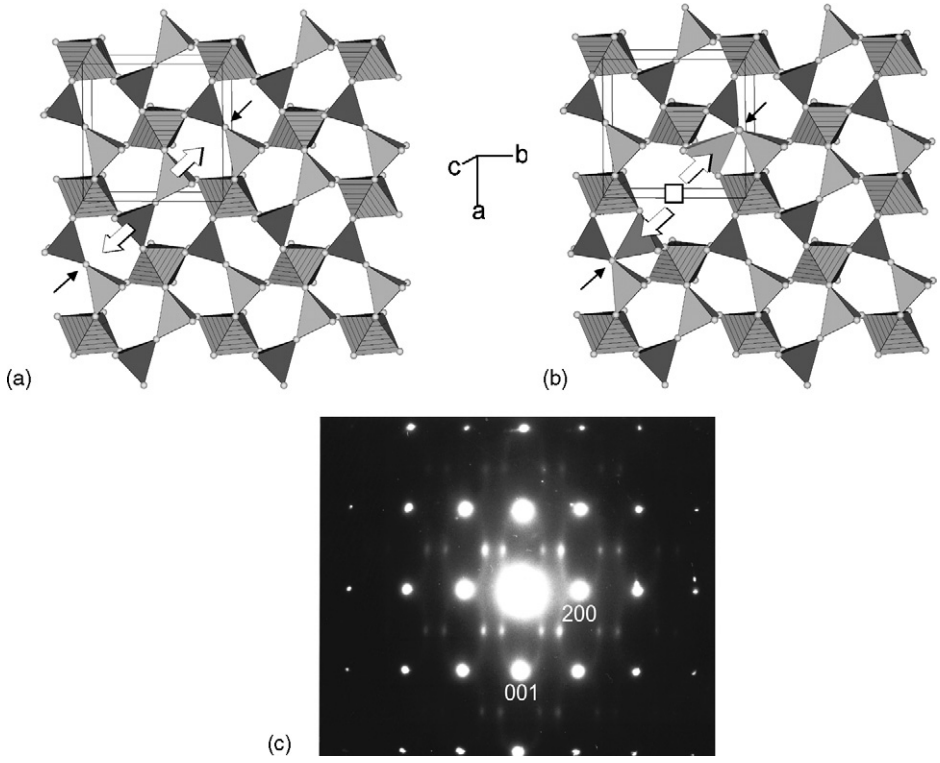

Fig. 8. Crystal structure of mullite as derived from that of sillimanite. View down the *c*-axis of (a) sillimanite and (b) mullite. Arrows show the structural modifications in going from sillimanite to mullite: big arrows indicate the migration directions of T cations, thin arrows point to the bridging O atom (usually designated as O(C)) becoming a tricluster O in mullite; □ = oxygen vacancy (from Fischer and Schneider).[3] (c) (*h* 0 *l*) electron diffraction pattern of 2/1-mullite showing superstructure reflections near $h = 1/3$ and $l = 1/2$ (from Rahman and Freimann).[11]

or to mixed crystals between these two. Actually there exists a miscibility gap between sillimanite ($x = 0.00$) and SiO_2-rich mullite ($x < 0.20$). The miscibility gap between sillimanite and mullite has been explained by the different formation conditions (sillimanite = moderate pressure, moderate temperature; mullite = low pressure, high temperature) and by the different ordering schemes of the phases. If mullite is a simple solid solution with little structural variations, the cell parameters should depend linearly on the Al_2O_3 content. The plot of the *a* lattice constant versus the Al_2O_3 content has frequently been used for the discussion of this dependence (Fig. 9), a summary of the literature is compiled in Fischer and Schneider.[3] It has been shown that the *a* lattice constant and the cell volume *V* of mullite actually increases linearly with the Al_2O_3 content, while *b* slightly and non-linearly decreases, and *c* non-linearly increases.[3,15] Extrapolation of the *a* and *b* curves towards $x = 0.00$ (i.e. 50 mol% Al_2O_3 content) results in the lattice constants of sillimanite. Continuing of the *a* and *b* curves towards higher *x*-values (higher Al_2O_3 contents and associated numbers of oxygen vacancies) yields a crossing point of both lines at $x \approx 0.67$ (≈80 mol% Al_2O_3, Fig. 9). Compounds with $a = b$ indeed do occur.[16,17] However, in spite of the coincidental identity of *a* and *b* lattice constants the phase is not tetragonal, but should better be designated as "pseudo-tetragonal". To be precise it should read "mullite with pseudo-tetragonal metric", since the symmetry clearly is orthorhombic. There exist few literature data on the crystal chemistry of the very Al_2O_3-rich mullites beyond the pseudo-tetragonal point ($x > 0.67$). Alumina phases with mullite-type structures (so-called ι-alumina) have been described in the literature and were believed to be either tetragonal or orthorhombic.[3] Re-examination of these phases, however, showed that they belong to the mullite-type aluminates rather than to mullite senso stricto.[3] The mullite with the highest Al_2O_3 content identified so far, was described by Schneider et al.[18] and Fischer et al.[19] This mullite has an Al_2O_3 content of 89 mol% Al_2O_3 ($x = 0.83$, which corresponds to a mullite composition of $Al_{5.65}Si_{0.35}O_{9.18}$), which is far beyond the pseudo-tetragonal point of the *a* and *b* curves. The crystal structure of the $a > b$-phases is difficult to understand, since the

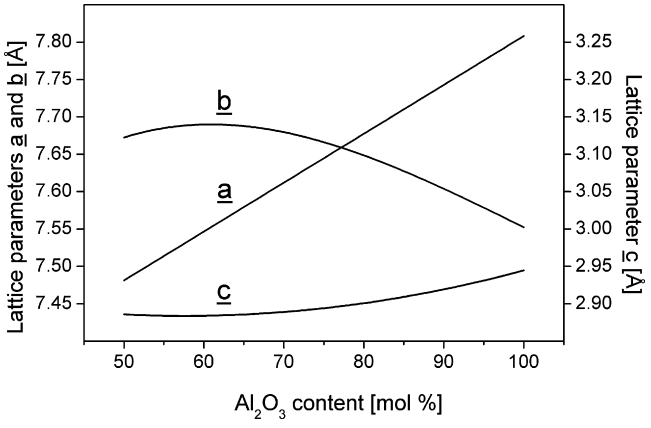

Fig. 9. Lattice constants *a*, *b* and *c* of mullite dependent from the Al_2O_3 content of the phase (from Fischer and Schneider).[3]

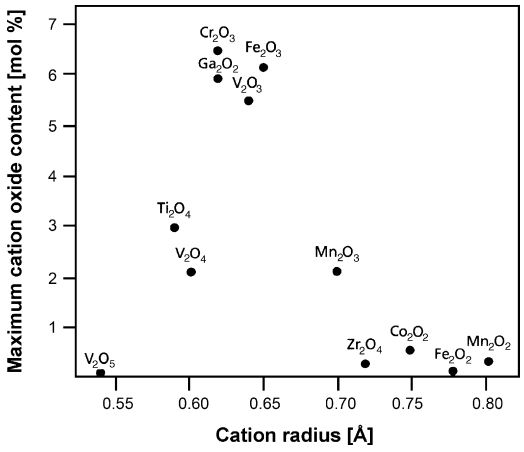

Fig. 10. Transition metal incorporation in mullite plotted vs. the radii of substituting cations. Ga incorporation is given for comparison (after Schneider).[21]

conventional structure model of mullite is restricted to $x \leq 0.67$ (<80 mol% Al_2O_3[8]), where all possible O(C) vacancies have formed. It has been mentioned that at compositions $x > 0.67$ some additional Al^{3+} ions are incorporated at interstitial sites of mullite structure.[8,9] Another approach to accommodate the additional Al was presented by Fischer et al.[19] It starts from the formation of T_4O groups (so-called tetraclusters), where four (!) tetrahedra are connected via one common oxygen atom, in spite of the fact that such a structural configuration should be highly unstable.

2.2. Foreign cation incorporation in mullite

Depending on synthesis temperature and atmosphere the mullite structure is able to incorporate a large variety of foreign cations. A review of the state of the art has recently been presented by Schneider.[20] In this chapter the essentials of foreign cation incorporation in mullite are given.

2.2.1. Transition metal incorporation

Dependent on synthesis temperature and atmosphere, mullite incorporates Ti^{3+}, Ti^{4+}, V^{3+}, V^{4+}, Cr^{3+}, Mn^{2+}, Mn^{3+}, Fe^{2+}, Fe^{3+} and Co^{2+} though in strongly differing amounts. The upper solubility limit is controlled by radii and oxidation states of the transition metal ions: Highest degrees of incorporation are observed for V^{3+}, Cr^{3+} and Fe^{3+} followed by Ti^{4+}. Only very low amounts of Mn^{2+}, Fe^{2+} and Co^{2+} ions can enter the mullite structure (Fig. 10).[21]

The transition metal ions preferably enter the octahedral position in mullite replacing Al, although details of the incorporation process can be quite different. Electron paramagnetic resonance (EPR) studies of Rager et al.[22] demonstrated that two differently distorted octahedral sites occur in the case of Ti^{3+} incorporation. Fe^{3+} also enters two slightly different octahedral sites, as could be proved by high-temperature Mössbauer investigations.[23] A low amount of tetrahedrally bound Fe^{3+} has also been identified by Mack et al.[23] Spectroscopic studies yielded evidence for a distribution of Cr^{3+} over the octahedral chains and an additional octahedral interstitial lattice site.[24] An alternative approach suggested the formation of Cr^{3+}–Cr^{3+} clusters in the octahedral chains in *c* direction.[3,25] Mn^{3+}-substituted mullites are characterized by strong changes of lattice spacings and associated high lattice strains. Both observations have been explained with Jahn–Teller distortion of Mn^{3+} in octahedral environment.[21,26]

The relatively large cation sizes and high octahedral but lower tetrahedral crystal field splitting parameters of most transition metal cations may explain their preference for octahedral coordination. Fe^{3+} and Mn^{2+} ions in the middle of the 3d transition metal series make an exception: These cations have stable d^5 electron configurations with nearly spherical symmetric charge distributions, similar to those of noble gases. Consequently Fe^{3+} and Mn^{2+} should exhibit no site preference and their incorporation behavior should mainly be controlled by the sizes of the cations. Actually a small amount of Fe^{3+} does enter the oxygen tetrahedra in mullite at high temperature. On the other hand, Mn^{2+} is obviously too large to be tetrahedrally incorporated in mullite.[21,26]

The entry of the relatively large transition metal cations into the oxygen octahedra at the place of Al should produce higher expansion for the *b*- than for the *a*-axis, because the most elastic bond of the octahedron (M–O(D)) lies to about 30° to either side of *b* (Fig. 8, see also Fig. 14). This type of expansion has actually been observed for V^{3+}, Mn^{3+} and Fe^{3+} substituted mullites (Table 3). The intense *a* expansion of Ti^{4+}-doped mullites was interpreted in terms of substitution of tetrahedral Si^{4+} by Al^{3+}, which occurs along with the octahedral incorporation of Ti^{4+} for charge compensation. The anomalously high *a* expansion of Cr^{3+}-substituted mullites may be due to partial entry of Cr^{3+} into interstitial structural sites or to the formation of clusters of CrO_6 octahedra.[24,25]

Besides electron configuration and size of cations, the amount of transition metal incorporation is dependent on the oxidation state of the ions. Maximum incorporations are observed for M^{3+} ions. This is reasonable, taking into account that octahedral transition metal incorporation is associated with a removal of Al^{3+} from the structure (Fig. 11). The entry of cations with deviating oxidation states, e.g., Ti^{4+} and V^{4+} is less favourable, since it requires simultaneous tetrahedral substitution of Si^{4+} by Al^{3+} in order to compensate for the excess positive charge. Due to the different fluxing character of the transition metal-doped alumino silicate melts from which mullite was formed, the microstructure of ceramics can vary dramatically (Fig. 12, for a more extended review see Schneider).[20]

2.2.2. Other foreign cation incorporation

Besides transition metals the mullite structure is able to incorporate a variety of other foreign cations, although in more or less high concentrations.[20] A maximum of about 12 wt.% Ga_2O_3 has been reported. According to microchemical relationships (Fig. 11), and due to the fact that Ga^{3+}-doped mullites display strongest incorporation produced expansion parallel to the crystallographic *b*-axis (Fig. 8) it has been suggested that Ga^{3+} substitutes Al^{3+} favorably at octahedral lattice positions. Griesser et al. (2006) mentioned that there exists a strong tendency of mullite to incorporate B^{3+}. B_2O_3 contents up to about 20 mol% have been reported (Fig. 13). According to microchem-

Table 3
Chemical composition and lattice parameters of mullites containing high amounts of transition metal cations

Composition (wt.%)	Method	Lattice parameters			
		a (Å)	b (Å)	c (Å)	V (Å^3)
Mullites containing transition metal cations					
Al_2O_3: 72.0; SiO_2: 24.5; TiO_2: 4.2	EMA	7.564	7.701	2.8931	168.5
Al_2O_3: 63.0; SiO_2: 28.2; V_2O_3: 8.7	XFA*	7.555	7.711	2.8995	168.9
Al_2O_3: 72.5; SiO_2: 24.0; V_2O_4: 3.5	XFA†	7.551	7.698	2.8936	168.2
Al_2O_3: 60.0; SiO_2: 28.4; Cr_2O_3: 11.5	EMA	7.570	7.712	2.9025	169.4
Al_2O_3: 68.4; SiO_2: 25.9; Mn_3O_4: 5.7	XFA‡	7.563	7.721	2.8828	168.3
Al_2O_3: 62.1; SiO_2: 27.4; Fe_2O_3: 10.3	EMA	7.574	7.726	2.9004	169.7
Reference mullite					
Al_2O_3: 71.2; SiO_2: 28.6	EMA	7.546	7.692	2.8829	167.3

Spectroscopic data and microchemical analyses suggest that samples marked *, † and ‡ contain essentially V^{3+}, V^{4+} and Mn^{3+}, respectively. Therefore, chemical compositions are given as V_2O_3, V_2O_4 and Mn_3O_4, respectively. EMA, electron microprobe analysis; XFA, X-ray fluorescence analysis. Data were taken from Fischer and Schneider[10].

ical studies alkali and alkaline earth cations are able to enter the mullite structure, though in small quantities. Due to its large cation size Na^+ may be only incorporated into the thermally expanded mullite structure at very high temperature (up to about 0.4 wt.% Na_2O).[27] Mullite incorporates up to about 0.5 wt.% MgO.[28] Both, Na^+ and Mg^{2+} incorporations decrease with temperature and are reciprocally correlated with the Al content of the phase. The observations have been interpreted in terms of an interstitial incorporation of Na^+ and a substitution of octahedral Al^{3+} ions by Mg^{2+}. Schneider[29] showed that Zr^{4+} enters the mullite structure in low amounts ($\leq$0.8 wt.% ZrO_2), and suggested that Zr^{4+} incorporation increases with temperature rather than with the bulk ZrO_2 content. Other foreign cations like Sn^{4+}, Mo^{3+}, and Eu^{2+} and Eu^{3+} have also been reported to enter the mullite structure though in small quantities.[30–32]

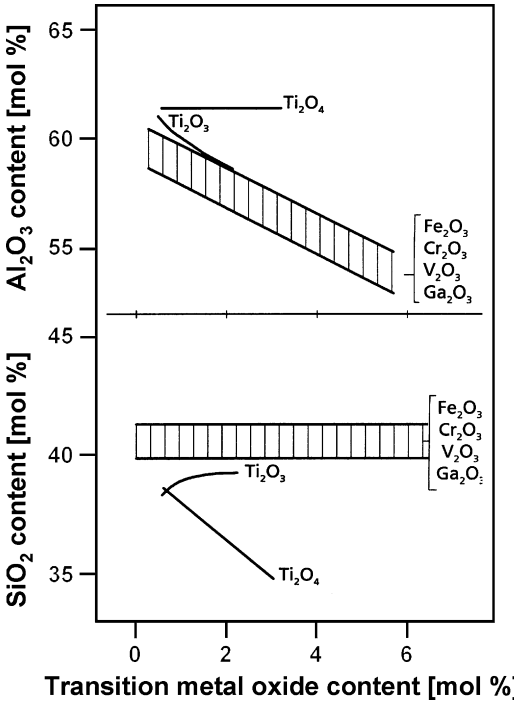

Fig. 11. Transition metal incorporation in mullite. Ti_2O_3, TiO_2, V_2O_3, Cr_2O_3 Mn_2O_3 and Fe_2O_3 are plotted vs. the Al_2O_3 and SiO_2 contents. Relationships for Ga_2O_3 are given for comparison. Note that there exists a reciprocal dependency between M_2O_3 and Al_2O_3 and M_2O_4 and SiO_2, respectively (from Schneider).[21]

3. Structure property relations of mullite

This chapter is devoted to correlations between the three-dimensional structural framework of mullite ("average structure") as outlined in the previous chapter and selected bulk properties like elasticity, thermal expansion, thermal conductivity, crystal growth, dissolution or corrosion, and atomic diffusion.

Furthermore, the influence of number and distribution of tetrahedral Al and Si atoms and associated oxygen vacancies ("real structure") on the behavior of mullite will be addressed. The discussion is based on data recently measured at the German Aerospace Center (DLR) or in cooperation with colleagues from other institutions. The paper does not intend to provide an overall review of the behavior of mullite. A broader discussion of the mechanical and thermal properties of mullite has recently been presented by Schneider.[33,34]

In the following the physical properties are referred to a Cartesian reference system $\{e_i\}$, the axes e_i of which are related to the axes of the crystallographic reference system according to $e_1//a$, $e_2//b$ and $e_3//c$.

3.1. Elastic properties

Elasticity plays a key role for the interpretation of the structure-property relationships, because elasticity exclusively arises from the interactions between the constituents of a crystal. The mean elastic stiffness is therefore closely related to the lattice energy, and the elastic anisotropy directly reflects the anisotropy of the bonding system of the crystal.

The elasticity of mullite can be explained by the behavior of sillimanite, because its structure provides a simple model of mullite (Fig. 7). The backbone of the crystal structure of sillimanite are bond chains parallel to [0 0 1], consisting of edge-sharing AlO_6 octahedra. Such a simple chain is in principle mechanically

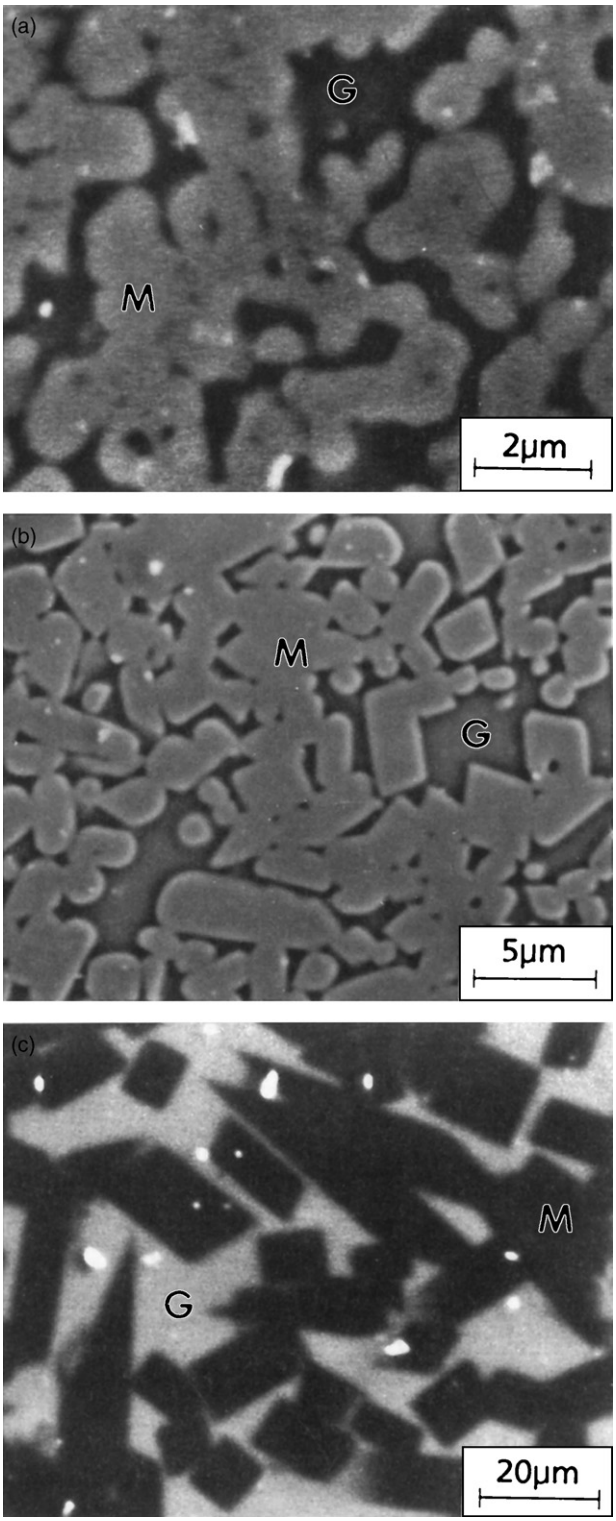

Fig. 12. Electron microprobe photographs of transition metal-doped mullite ceramics. (a) V_2O_3-rich ceramic, with mullite containing 8.7 wt.% V_2O_3. (b) Cr_2O_3-rich ceramic, with mullite containing 11.5 wt.% Cr_2O_3. (c) Fe_2O_3-rich ceramic, with mullite containing 10.3 wt.% Fe_2O_3. Note the different shapes and sizes of crystals. M = mullite, G = glass (from Schneider et al.).[21]

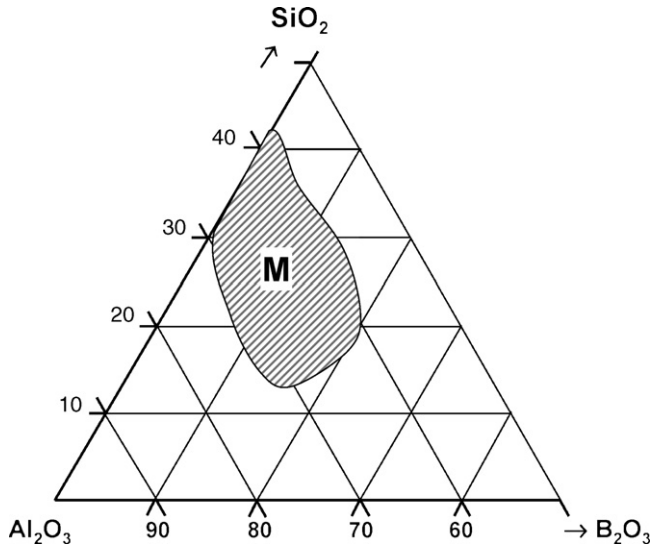

Fig. 13. B_2O_3 incorporation in mullite (M). Note the extended mixed crystal range (after Griesser, unpublished results).

soft, because longitudinal deformations can be easily achieved by tilting of neighbored octahedra around the common edge. In the case of sillimanite the octahedral chains are reinforced by AlO_4 and SiO_4 tetrahedra, which connect the free tips of adjacent octahedra (see Fig. 7). This structural arrangement prevents any tilt of the octahedra, thus leading to an elastically rigid composite chain. Perpendicular to [0 0 1] the structure is much softer. Relationships parallel to the *a*- and *b*-axes are schematically drawn in Fig. 14. Both directions are characterized by alternating sequences of relatively "stiff" tetrahedra and "soft" octahedra. A closer inspection reveals that the longest and thus weakest and most elastic Al–O(D) bond in mullite lies to about 30° to the *b*-axis but to about 60° to *a*-axis. Consequently, the anisotropy of the longitudinal elastic stiffness of sillimanite is characterized by $c_{33} \gg c_{11} > c_{22}$ (Table 4). The direction of the stiffness maximum coincides with the direction of the structurally domi-

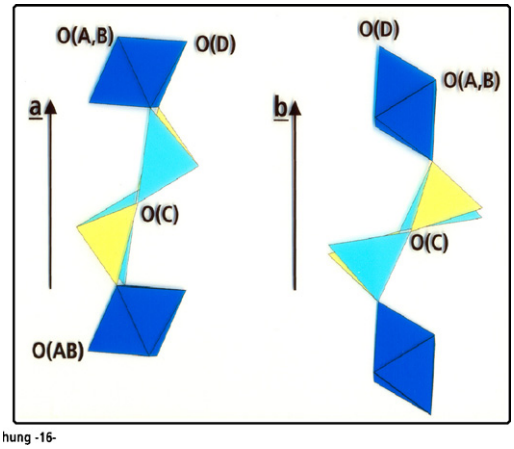

Fig. 14. Schematic and simplified drawing of the octahedron–tetrahedron interlinking in sillimanite (and mullite) parallel to the *a* and *b* axes. Note that parallel to the *a*-axis the tetrahedral double chains are linked to the relatively short octahedral Al–O(A, B) bond (less elastic), whereas parallel *b* they are linked to the relatively long octahedral Al–O(D) bond (more elastic).

Table 4
Elastic properties of mullite and sillimanite

	Sillimanite[35]	2/1-Mullite[39]	2.5/1-Mullite[37]
Composition x	0.00	0.39	0.50
Single crystal properties			
P (g cm^{-3})	3.241	3.126	3.110
c_{11} (GPa)	287.3	279.5	281.9
c_{22} (GPa)	231.9	234.9	244.2
c_{33} (GPa)	388.4	360.6	363.6
c_{44} (GPa)	122.4	109.5	111.7
c_{55} (GPa)	80.7	74.9	78.2
c_{66} (GPa)	89.3	79.9	79.2
c_{12} (GPa)	94.7	103.1	105.1
c_{13} (GPa)	83.4	96.1	100.3
c_{23} (GPa)	158.6	135.6	142.3
c (GPa)	170.7	163.8	167.4
$\partial c_{11}/\partial T$ (MPa K^{-1})		−28.1	−29.2
$\partial c_{22}/\partial T$ (MPa K^{-1})		−29.6	−29.7
$\partial c_{33}/\partial T$ (MPa K^{-1})		−28.2	−28.6
$\partial c_{44}/\partial T$ (MPa K^{-1})		−8.24	−7.9
$\partial c_{55}/\partial T$ (MPa K^{-1})		−6.09	−6.5
$\partial c_{66}/\partial T$ (MPa K^{-1})		−9.00	−10.1
$\partial c_{12}/\partial T$ (MPa K^{-1})		−15.8	−16.1
$\partial c_{13}/\partial T$ (MPa K^{-1})		−9.1	−6.8
$\partial c_{23}/\partial T$ (MPa K^{-1})		−6.3	−8.1
Isotropic polycrystal properties (average of Voigt and Reuss model)			
c_{11}^{iso} (GPa)	295.2	284.8	290.9
c_{12}^{iso} (GPa)	109.5	111.2	114.9
$c_{44}^{iso} = (c_{11}^{iso} - c_{12}^{iso})/2$ (GPa)	92.9	86.8	88.0
B_{iso} (GPa)	171.4	169.1	173.6
$\partial c_{11}^{iso}/\partial T$ (MPa K^{-1})		−28.6	−29.2
$\partial c_{12}^{iso}/\partial T$ (MPa K^{-1})		−11.7	−11.6
$\partial c_{44}^{iso}/\partial T$ (MPa K^{-1})		−8.49	−8.81

ρ, density; c_{ij}, elastic stiffness; c, mean elastic stiffness; c, $\sum c_{ij}/9$; B, bulk modulus; $\partial c_{ij}/\partial T$, linear temperature coefficient of the elastic stiffness. The x-value refers to the general composition of mullite $Al_{4+2x}Si_{2-2x}O_{10-x}$, x giving the number of oxygen vacancies per unit cell.

nant composite chains, whereas the longitudinal elastic stiffness within the (0 0 1) plane is on the average about 33% smaller than that parallel to [0 0 1]. Although the elastic anisotropy of sillimanite within the (0 0 1) plane is small the results obtained from Brillouin spectroscopy experiments[35] agree well with those derived from X-ray diffraction-based compressibility measurements. Yang et al.[36] showed that the compressibility is actually highest along to the longest and most elastic octahedral Al–O(D) bond, whereas the compressibilities along to the shorter and stronger Al–O(A) and Al–O(B) bonds are smaller (Fig. 15).

The elastic behavior of mullite is qualitatively very similar to that of sillimanite (Fig. 16). However, partial substitution of Si^{4+} by Al^{3+} occurs, introducing oxygen vacancies for charge compensation. This causes a weakening of the tetrahedral double chains due to the substitution of Si^{4+} by the larger Al^{3+} ion. Moreover, it leads to a reduction of the number of tetrahedra reinforcing the octahedral chains. As a consequence, the c_{33} of 2/1-mullite is about 8% smaller than that of sillimanite. In directions perpendicular to c-axis only minor differences are observed in the elastic properties of both crystal species.[37–39] There is also a similarity with the elastic constants of the mullite-type

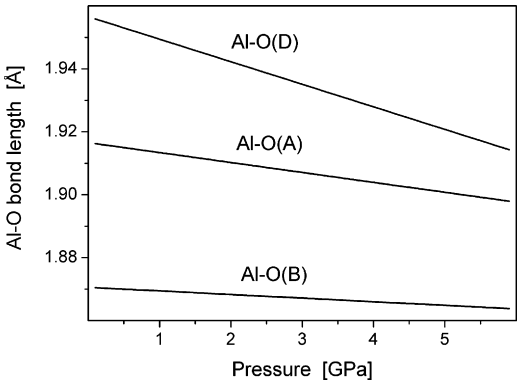

Fig. 15. Compressibility of the octahedron of sillimanite. Shown are Al–O bond lengths dependent on the applied pressure. Note that the longest Al–O(D) bond displays the highest compressibility (after Yang et al.).[36] The octahedral chains in mullite are very similar to those in sillimanite, although Al–O(A) and Al–O(B) bond lengths are equal in mullite and therefore are designated as Al–O(A, B).

phase $Bi_2Ga_4O_9$, the elastic properties of which are essentially controlled by the strong octahedral chains.[55]

According to Schreuer et al.[39] the elastic constants of 2/1-mullite decrease almost linearly between room temperature and 1400 °C. The thermoelastic constants $T_{ij} = \mathrm{d} \log c_{ij}/\mathrm{d}T$ are within the typical range of many silicates. The anisotropy of the thermoelastic behavior is closely correlated to the bonding system of mullite. At room temperature the angle O(D)–T–O(D) of the bridging bonds of the tetrahedra is larger than the ideal tetrahedral angle, i.e., the bonds are already pre-stressed. With increasing temperature the larger expansion of the octahedra produces an increasing stress on the tetrahedra. This leads to an additional contribution to the stiffness of the principal bond chains along [0 0 1] that partially compensates for the decreasing bonding interactions because of increasing thermal motion. The thermoelastic behavior of mullite is therefore characterized by $|T_{33}| < |T_{11}|$, $|T_{22}|$ and $|T_{12}| > |T_{13}|$, $|T_{23}|$.

3.2. Thermal conductivity

Except at very high temperatures where photons may play an important role, thermal energy in insulating materials is mainly transported by lattice vibrations. According to a simple model proposed by Debye the thermal conductivity λ is given by $\lambda = 1/3 C_v v^2 \tau$. Here C_v denotes the contribution of the phonons to the specific heat capacity, v the phonon velocity and τ is the phonon collision rate. If we neglect dispersion effects the effective elastic stiffness $c = \rho v^2$ (ρ density) associated with v is related to the longitudinal elastic stiffness along the propagation direction of the phonon. The close correlation between thermal conductivity and longitudinal elastic stiffness is clearly evident in compounds with one predominant bond chain. In rutile for example the maximum of both the longitudinal elastic stiffness and the thermal conductivity occur along the direction of the strongest bond chain parallel to the tetragonal axis. On the other hand, structurally more isotropic phases like α-alumina display only little anisotropy of the thermal conductivity.[40,41] Due to the three-dimensional framework of very strong covalent bonds diamond belongs not only to the stiffest materials known to date

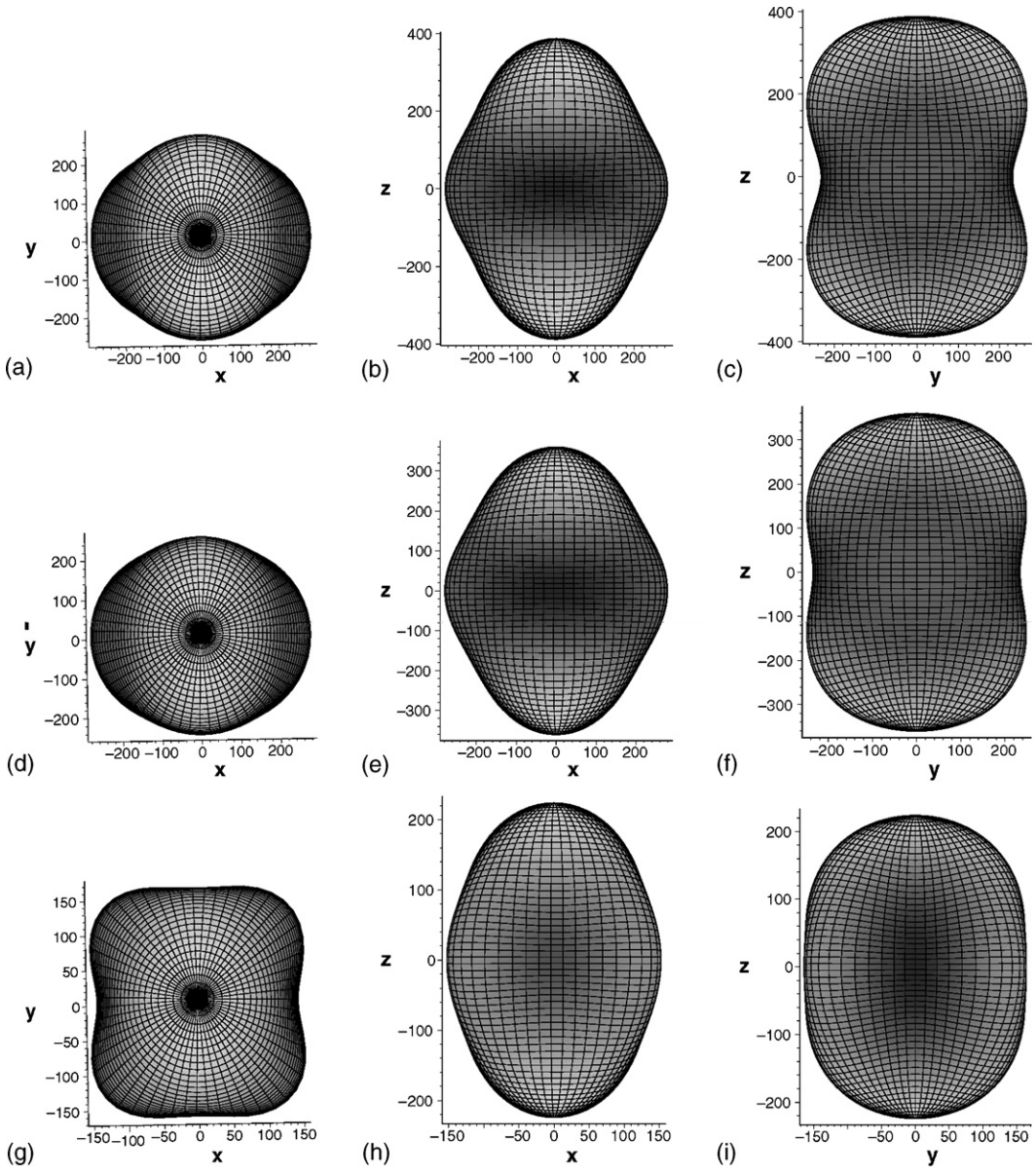

Fig. 16. Representation surface of longitudinal elastic stiffness $c'_{1111} = u_{1i}u_{1j}u_{1k}u_{1l}c_{ijkl}$ (u_{1i} direction cosine) of sillimanite ((a–c) Vaughan and Weidner[35], 2/1-mullite; (d–f) Schreuer[39]) and structurally related $Bi_2Ga_4O_9$ ((g–i) Schreuer[55]). Each row shows views of the corresponding representation surface along [0 0 1], [0 1 0] and [1 0 0]. The labelling *X*, *Y*, *Z* of the axes corresponds to the axes e_1, e_2 and e_3 of the Cartesian reference system. Units are in GPa.

but also possesses highest thermal conductivity. In the case of orthorhombic 2/1-mullite the relation $c_{33} \gg c_{11} > c_{22}$, therefore implies $\lambda_{33} \gg \lambda_{11} > \lambda_{22}$ in full agreement with experiment[42] (Fig. 17).

3.3. Thermal expansion

The coefficients of thermal expansion α_{ij} belong to the crystal properties of $Al_{4+2x}Si_{2-2x}O_{10-x}$ phases most often studied by different authors. Although the high-resolution X-ray and neutron diffractometric[43,44] and dilatometric measurements[39] revealed a significant temperature dependence of the thermal expansion coeffcients, and α_{ij} are assumed to be constant in first approximation between 300 and 1000 °C and above 1000 and up to 1600 °C (Table 5).

In stable crystal species far from structural phase transitions often the direction of the maximum of the longitudinal elastic stiffness coincides with the one of minimal thermal expansion and vice versa. However, in the case of sillimanite and mullite this empirical rule holds only within the (0 0 1) plane. All measurements yielded highest expansion parallel to the crystallographic *b*-axis, but considerably lower ones parallel *a*-axis. This is understandable, taking into account that the long and most compliant octahedral Al–O(D) bond does allow high-temperature-induced stretchings. Things are less clear along the *c*-axis where the strong bond chains suggest low expansion coefficients. This, however, has not been observed. In the contrary: The α_{33} value tends to be nearly as high as α_{22}, or can be even higher. Although the effect is not fully understood yet, the following explanation may be taken into account.

Table 5
Thermal expansion coefficients of undoped and Cr-doped mullite (10 wt.% Cr_2O_3)

Compound	Composition x	Method	Temperature range (°C)	Linear thermal expansion coefficients ($\times 10^{-6}\,°C^{-1}$)				Reference
				α_{11}	α_{22}	α_{33}	α_V	
Sillimanite	0	XRD	25–900	2.3	7.6	4.8	14.7	Schneider[34]
Mullite (undoped)	0.24	XRD	300–900	3.9	7.0	5.8	16.7	Schneider and Eberhard[43]
Mullite (undoped)	0.25	XRD, ND	300–1000	4.1	6.0	5.7	15.8	Brunauer et al.[44]
Mullite (undoped)	0.25	ND	1000–1600	6.8	9.3	6.3	22.4	Brunauer et al.[44]
Mullite (undoped)	0.39	XRD	300–900	4.1	5.6	6.1	15.8	Schneider and Eberhard[43]
Mullite (undoped)	0.39	DIL	300–1000	4.5	6.1	7.0	17.6	Schreuer et al.[39]
Mullite (undoped)	0.39	DIL	1000–1400	6.2	7.3	6.9	20.4	Schreuer et al.[39]
Mullite (Cr-doped)	0.21	ND	300–1000	3.6	5.9	5.2	14.7	Brunauer et al.[44]
Mullite (Cr-doped)	0.21	XRD	300–1000	3.1	6.2	5.6	14.9	Schneider and Eberhard[43]
Mullite (Cr-doped)	0.21	ND	1000–1600	5.8	11.0	6.1	22.9	Brunauer et al.[44]

The coefficients were obtained by fitting first-order polynomials to corresponding experimental data. $\alpha_V \approx \alpha_{11} + \alpha_{22} + \alpha_{33}$ is the linear coefficient of volume expansion. XRD: high-temperature X-ray diffraction; ND: high-temperature neutron diffraction; DIL: high-temperature single crystal dilatometry. The x-value refers to the general composition of mullite $Al_{4+2x}Si_{2-2x}O_{10-x}$, x giving the number of oxygen vacancies per unit cell.

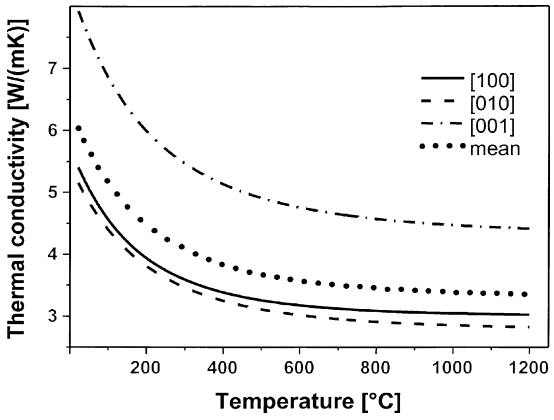

Fig. 17. Temperature-dependent evolution of the thermal conductivity of 2/1-mullite single crystal parallel to the a ([1 0 0]), b [(0 1 0)], and c ([0 0 1]) axes. Note the anisotropy of the thermal conductivity with the relatively high conductivity parallel c (after Hildmann and Schneider[42]).

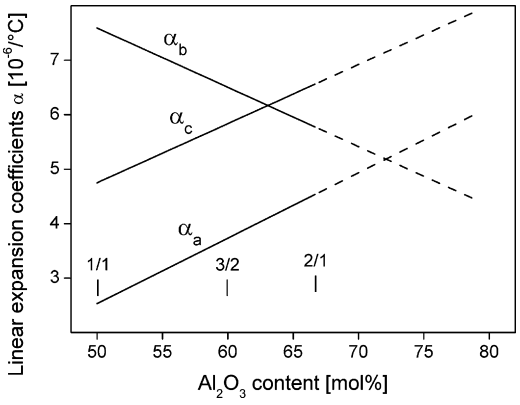

Fig. 18. Thermal expansion coefficients α_a, α_b, and α_c of mullite parallel to the a ([1 0 0]), b ([0 1 0]) and c ([0 0 1]) axes plotted vs. the Al_2O_3 content of mullite. Symbols 1/1, 3/2 and 2/1 refer to sillimanite ($x = 0.00$), 3/2-mullite ($x = 0.25$) and 2/1-mullite ($x = 0.40$, after Schneider and Eberhard[43]).

The violation of the above-described general rule in mullite is possibly caused by the special arrangement of octahedra and tetrahedra within the principal bond chains parallel to [0 0 1]. Increasing thermal motion leads to an expansion of the octahedra. Correspondingly, the O(D)–T–O(D) angles of the connected tetrahedra increase and the tetrahedrally coordinated cations move towards the octahedral chains resulting in a negative contribution to the thermal expansion within the plane perpendicular to the chains. Thus α_{33} appears relatively large compared to α_{11} and α_{22}.

The plot of the Al_2O_3 content versus the thermal expansion coefficients α_{ij} of mullite yields interesting results (Fig. 18). With increase of the x-value of $Al_{4+2x}Si_{2-2x}O_{10-x}$ (corresponding to the number of oxygen vacancies and the Al_2O_3 content), the thermal expansion coefficients of α_{11} and α_{33} of mullite increase while that of α_{22} decreases. The increase of α_{33} correlates with the increasing number of oxygen vacancies: Thereby

Table 6
Octahedral M–O bond lengths in sillimanite and mullite dependent on the composition

	Sillimanite[6]	3/2-Mullite[9]	2/1-Mullite[7]	9/1-Mullite[19]
Composition x	0.00	0.25	0.40	0.89
Bond length (Å)				
Al–O(A, B)	1.885 (mean)	1.896	1.894	1.942
Al–O(D)	1.957	1.942	1.937	1.945
Bond length ratio				
Al–O(A, B)/Al–O(D) ratio	0.963	0.976	0.978	0.999

The x-value refers to the general composition of mullite $Al_{4+2x}Si_{2-2x}O_{10-x}$, x giving the number of oxygen vacancies per unit cell. In sillimanite Al–O(A) and Al–O(B) are 1.919 and 1.861 Å, respectively.

the stabilization of the octahedral chains by the tetrahedral double chains is gradually reduced. This has the consequence that the structure becomes "softer" and more expandable in *c*-axis direction. The increase of α_{11} and the decrease of α_{22} with x, on the other hand, can be associated with the increase of the relatively short octahedral Al–O(A, B) bonds (becoming more elastic) and the slight shortening of the initially longer octahedral Al–O(D) bonds (becoming less elastic, see Table 6). The extrapolation of α_{11} and α_{22} towards higher x-values yields a crossover of both curves at $x > 0.60$, corresponding approximately to the pseudo-tetragonal composition of mullite ($x \approx 0.67$).

Cr^{3+}- and Fe^{3+}-substituted mullites display lower thermal expansions than undoped mullite[43,44] (see also Table 5). Obviously, the substitution of the octahedral Al^{3+} ions by the larger Cr^{3+}- and Fe^{3+}-ions causes a pre-stressing of the mullite structure, which works against further expansion with the increase of temperature.

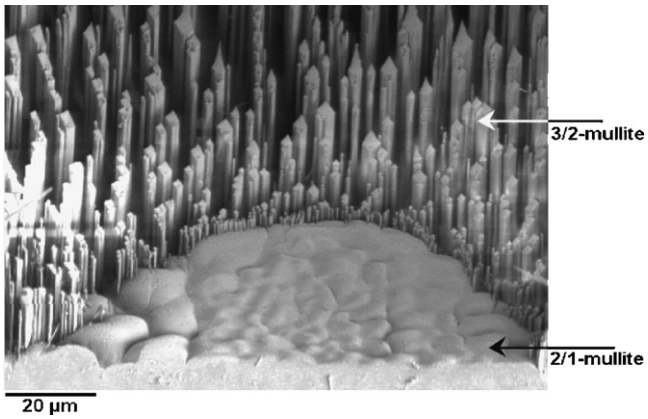

Fig. 19. Fast acicular *c*-axis growth of mullite in a Na_2O–SiO_2 glass/(0 0 1) mullite reaction couple. The sample was etched with a HF/HCl solution (from Schmücker et al.[46]).

3.4. Crystal growth, dissolution and corrosion

Mullite crystals grown in coexistent alumino silicate melts usually display acicular morphology with the needle axis parallel to the crystallographic *c*-axis (Fig. 19). This observation may be explained by the periodic bond chain (PBC) model first mentioned by Hartman and Perdok.[45] According to this approach the morphology of a crystal grown closely to thermodynamic

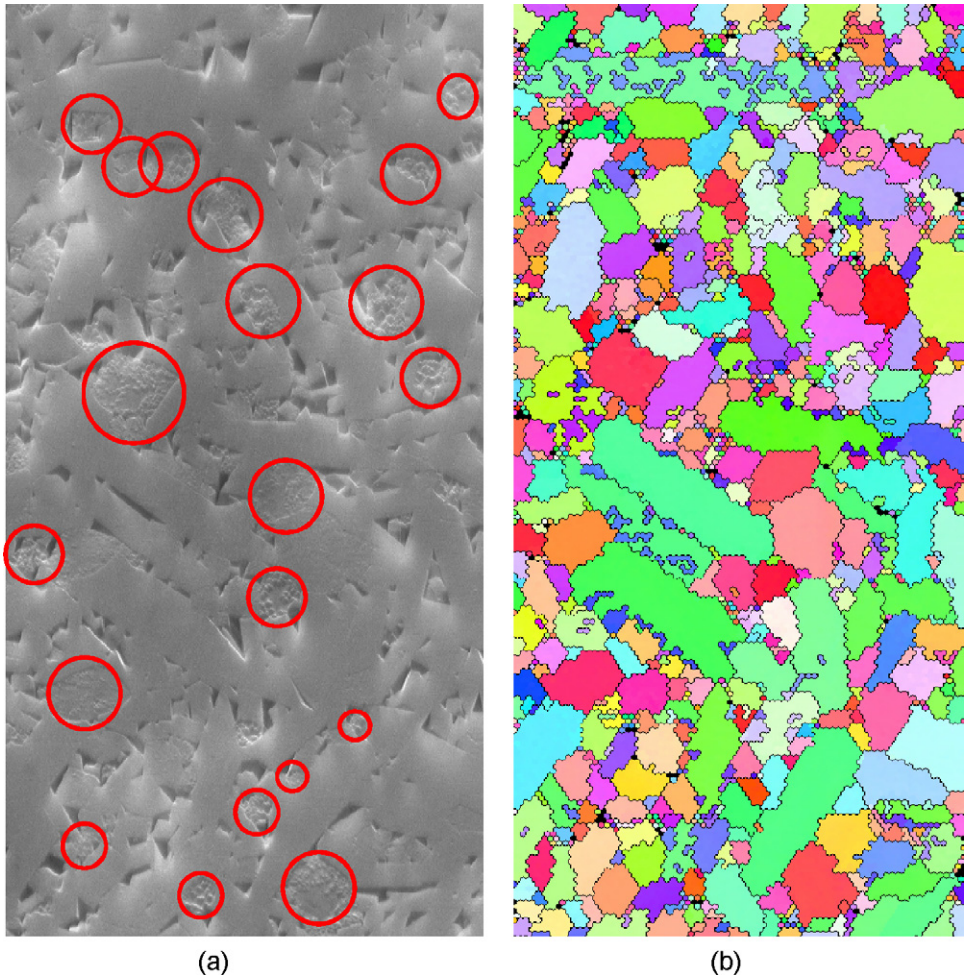

Fig. 20. Corrosion of a polycrystalline mullite ceramic after treatment at 1200 °C in H_2O gas atmosphere ($p_{H_2O} = 1$ bar) and a gas streaming velocity of 10 m s^{-1} for 4 h. (a) Scanning electron micrograph with strongly (circles) and less corroded mullite sections. (b) Electron back scatter diffraction (EBSD) pattern of the section shown under (a). The dark crystal sections are those having their *c* axes nearly perpendicular to the image plane, i.e., planes near to (0 0 1) (from Schmücker et al.[47]).

equilibrium state is related to a system of strong periodic bond chains, represented by corresponding PBC-vectors. Faces parallel to lattice planes spanned by two or more strong PBC-vectors exhibit lower specific surface energies σ than faces which cut one or more strong PBC-vectors. In crystals like mullite possessing one preferential direction **u** of strong bond chains we expect for faces with normals **h** the relation $\sigma(\mathbf{h}||\mathbf{u}) \gg \sigma(\mathbf{h}\infty\mathbf{u})$. In the case of mullite with its strongly bound chains parallel to *c*-axis it suggests a higher surface energy σ in (0 0 1) than in $\{h\,k\,0\}$ planes. On the other hand, crystal growth should be enhanced parallel *c*-axis, which actually comes true. Therefore, long-prismatic to acicular morphology with dominant pinacoids $\{1\,0\,0\}$, $\{0\,1\,0\}$ and/or prisms $\{h\,k\,0\}$ is most favorable for mullite crystals grown from alumino silicate melts.[46]

Mullite dissolution and corrosion can be roughly interpreted as an inverse crystal growth process. In accordance with the PBC theory water vapor corrosion experiments show that lattice planes perpendicular (i.e., (0 0 1)) or nearly perpendicular to the *c*-axis of mullite show the strongest corrosion (Fig. 20). The wetting behavior of mullite single crystals also fits well in this picture: The wetting angle on (0 0 1) is lowest (highest surface energy), followed by (1 0 0) and (0 1 0) (lowest surface energy).[48]

3.5. Atomic diffusion

Diffusion coefficients of O, Al and Si parallel to the [0 1 0] and [0 0 1] of mullite are plotted in Fig. 21 at temperatures above 1200 °C.[49–52] If the structural oxygen vacancies in mullite are part of the path ways for Al, Si, and O migration, the diffusion coefficients parallel *c*-axis should be higher than the corresponding ones parallel to *b*-axis. This follows from the fact that the density of structural oxygen vacancies occurring along [0 0 1] is higher than perpendicular to it. However, there is no experimental evidence for any anisotropic atom diffusion (Fig. 21). On the contrary the isotropic character of diffusion suggests that the pre-existing structural vacancies in mullite do not directly serve for O, Al and Si atom migration. Obviously "conductional" vacancies have to be formed in order to enable atom diffusion in mullite. Whether activated structural vacancies can become "conductional" ones, or whether other vacancies have to be newly built is not clear.

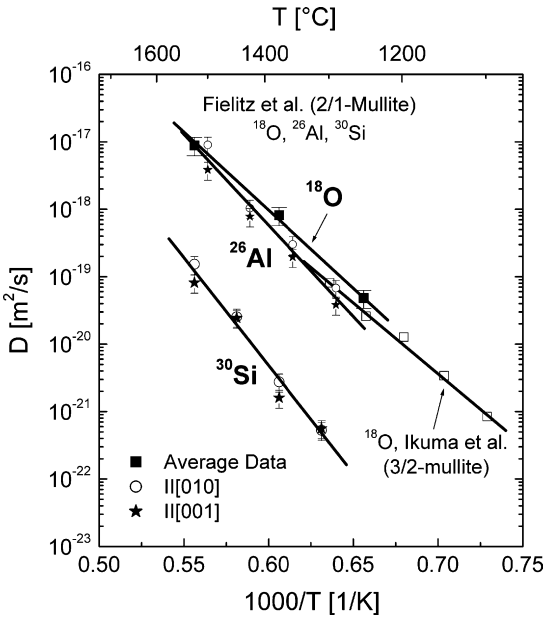

Fig. 21. Temperature-dependent ^{18}O, ^{30}Si and ^{26}Al diffusion in 2/1-mullite single crystals parallel to the *b* ([0 1 0]) and *c* ([0 0 1]) axes. Note that the atomic diffusion of species is isotropic with respect to the mullite crystal structure. *T*, temperature; *D*, diffusion coefficients (after Fielitz et al.[52]).

3.6. Order/disorder transformations

Despite of the great experimental efforts to explore the structural and physical properties of mullite, it is still under debate whether mullite undergoes a phase transition at high temperatures. Without doubt the temperature evolution of certain physical properties of mullite show weak but with respect to experimental error significant and reproducible anomalies in the temperature range between about 1000 and 1200 °C. Examples are

(i) a step-like increase of about 10% in the specific heat capacity C_p (no latent heat) at about 1200 °C[53,54] (Fig. 22);

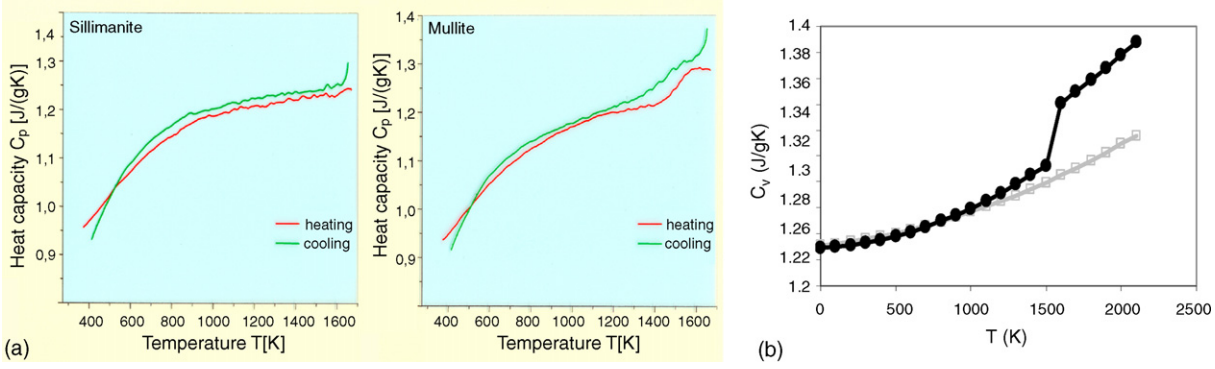

Fig. 22. Temperature-dependent evolution of the heat capacity C_p of mullite. (a) Experimentally determined curves of mullite (right) and sillimanite (left), both for heating-up and cooling-down. Note the high-temperature anomalies occurring in the curves of mullite but not of sillimanite.[53] (b) Calculated heating-up curves for mullite (full symbols) and sillimanite (open symbols). Note again the occurrence of the high-temperature anomaly in the curve of mullite but not of sillimanite.[54]

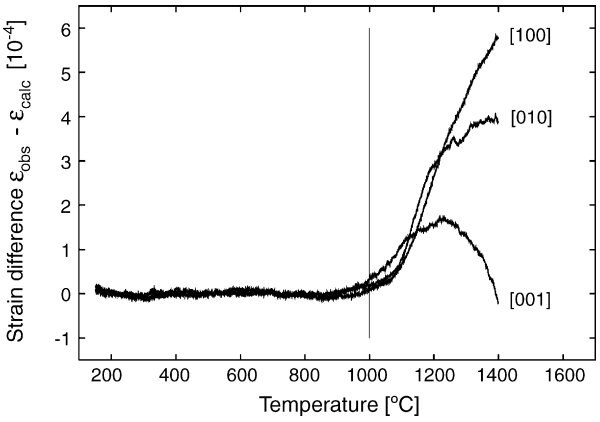

Fig. 23. Temperature-dependent strain differences $\varepsilon_{obs} - \varepsilon_{calc}$ along to the a ([1 0 0]), b ([0 1 0]) and c ([0 0 1]) axes (from Schreuer et al.[39]). Note the strong dicontinuities above about 1000 °C. ε_{obs}, observed value; ε, calculated value.

(ii) a step in all independent coefficients of thermal expansion α_{ii} above about 1100 °C[39] (Fig. 23);
(iii) an accelerated softening of the elastic shear resistances c_{44}, c_{55} and c_{66} above about 1000 °C, which is accompanied by rapidly increasing ultrasound attenuation.[39]

In summary these anomalies are not characteristic for any particular type of structural phase transitions. They rather resemble the behavior of a glass below and above its glass transition point. With this idea in mind Hildmann and Schneider[53] interpreted the anomalous effects by an onset of hoppings of tetrahedral Al between adjacent T (tetrahedral double chain cation position) and T* sites (tetrahedral tricluster cation position), and of O atoms between O(C) (bridging oxygen of tetrahedral double chains) and □ (oxygen vacancies). Below about 1000 °C tetrahedral Al and □ are believed to occur in a frozen-in partially ordered state ("static state"). Above 1000 °C dynamic site-exchange processes between T and T* and between O(C) and □ may take place ("dynamic state", Fig. 24). It is important to state that the proposed "static ↔ dynamic" transitions do not involve any change of the ordering schemes of vacancies and of the tetrahedral Al and Si. The authors believe instead that O hoppings and cation displacements oscillate around their initial sites. This should give rise to a broadening of superstructure reflections but not to a principle change of the diffraction pattern. The model of the phase transformation thus is not in contradiction to the observation of Paulmann[13] who deduced from diffraction experiments that the ordering scheme of oxygen vacancies and correlated Al and Si distributions in mullite persist up to the melting point of the phase. Cooling down the system below 1000 °C freezes-in the actual structural environments. Thus at room temperature the local structural arrangement in the average corresponds to those of the initial high-temperature ("dynamic") state, although it can vary locally.

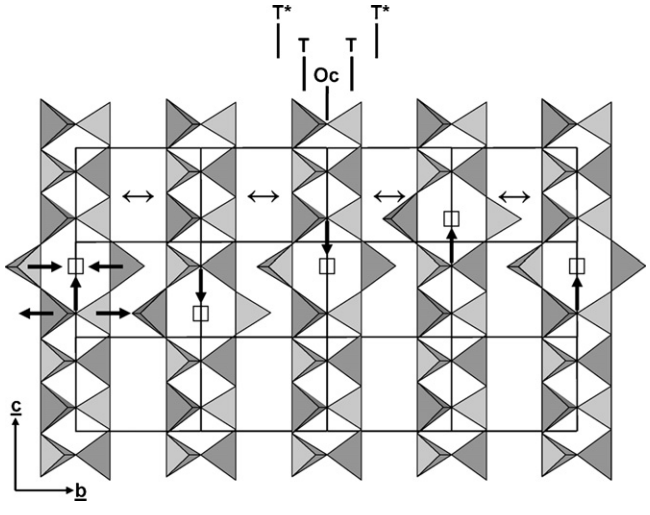

Fig. 24. Suggested mechanism of the high-temperature transformation of mullite. Hoppings of O between O(C) and □ sites and associated re-arrangement of T and T* sites ("dynamic state") are believed to occur. At low temperature the □ and T, T* sites are in a frozen-in partially ordered state ("static state"). T, tetrahedral double chain cation site; T*, tetrahedral tricluster cation site; O(C), oxygen bridging tetrahedral double chains; □, oxygen vacancy formed by removal of O(C).

References

1. Winkler, H. G. F., *Petrogenesis of Metamorphic Rocks* (*3rd ed.*). Springer, New York, 1974.
2. Tröger, W. E., *Optische Bestimmung der gesteinsbildenden Minerale*. Teil 2, Textband, Schweizerbart, Stuttgart, 1969.
3. Fischer, R. X. and Schneider, H., The mullite-type family of crystal structures. In *Mullite*, ed. H. Schneider and S. Komarneni. Wiley-VCH, Weinheim, 2005, pp. 1–46.
4. Schmücker, M. and Schneider, H., Mullite-type gels and glasses. In *Mullite*, ed. H. Schneider and S. Komarneni. Wiley-VCH, Weinheim, 2005, pp. 93–128.
5. Fischer, R. X., Schneider, H. and Voll, D., Formation of aluminum rich 9:1 mullite and its transformation to low alumina mullite upon heating. *J. Eur. Ceram. Soc.*, 1996, **16**, 109–113.
6. Burnham, C. W., Refinement of the crystal structure of sillimanite. *Z. Krist.*, 1963, **118**, 127–148.
7. Sadanaga, R., Tokonami, M. and Takeuchi, Y., The structure of mullite, $2Al_2O_3{\cdot}SiO_2$, and relationship with the structures of sillimanite and andalusite. *Acta Cryst.*, 1962, **15**, 65–68.
8. Angel, R. J. and Prewitt, C. T., Crystal structure of mullite: a re-examination of the average structure. *Am. Miner.*, 1986, **71**, 1476–1482.
9. Angel, R. J., McMullan, R. K. and Prewitt, C. T., Substructure and superstructure of mullite by neutron diffraction. *Am. Miner.*, 1991, **76**, 332–342.
10. Saalfeld, H. and Guse, W., Structure refinement of 3:2-mullite ($3Al_2O_3{\cdot}2SiO_2$). *N. Jb. Miner. Mh.*, 1981, **H4**, 145–150.
11. Rahman, S. and Freimann, S., The real structure of mullite. In *Mullite*, ed. H. Schneider and S. Komarneni. Wiley-VCH, Weinheim, 2005, pp. 46–70.
12. Schmücker, M., MacKenzie, K. J. D., Smith, M. E., Carroll, D. E. and Schneider, H., AlO_4/SiO_4 distribution in tetrahedral double chains of mullite. *J. Am. Ceram. Soc.*, 2005, **88**, 2935–2937.
13. Paulmann, C., Study of oxygen vacancy ordering in mullite at high temperatures. *Phase Trans.*, 1996, **59**, 77–90.
14. Burnham, C. W., Composition limits of mullite and the sillimanite—mullite solid solution problem. *Carnegie Inst., Washington, Yearb.*, 1964, **63**, 223–227.
15. Rehak, P., Kunath-Fandrei, G., Losso, P., Hildmann, B., Schneider, H. and Jäger, C., Study of the Al coordination in mullites with varying Al:Si ratio by ^{27}Al NMR spectroscopy and X-ray diffraction. *Am. Miner.*, 1998, **83**, 1266–1276.
16. Ossaka, J., Tetragonal mullite-like phase from co-precipitated gels. *Nature*, 1961, **191**, 1000–1001.
17. Schneider, H. and Rymon-Lipinski, T., Occurrence of pseudotetragonal mullite. *J. Am. Ceram. Soc.*, 1988, **71**, C162–C164.

18. Schneider, H., Fischer, R. X. and Voll, D., Mullite with lattice constants $a > b$. *J. Am. Ceram. Soc.*, 1993, **76**, 1879–1881.
19. Fischer, R. X., Schneider, H. and Schmücker, M., Crystal structure of Al-rich mullite. *Am. Miner.*, 1994, **79**, 983–990.
20. Schneider, H., Foreign cation incorporation in mullite. In *Mullite*, ed. H. Schneider and S. Komarneni. Wiley-VCH, Weinheim, 2005, pp. 70–93.
21. Schneider, H., Transition metal distribution in mullite. *Ceram. Trans.*, 1990, **6**, 135–158.
22. Rager, H., Schneider, H. and Bakhshandeh, A., Ti^{3+} centres in mullite. *J. Eur. Miner. Soc.*, 1993, **5**, 511–514.
23. Mack, D. E., Becker, K. D. and Schneider, H., High-temperature Mössbauer study of Fe-substituted mullite. *Am. Miner.*, 2005, **90**, 1078–1083.
24. Rager, H., Schneider, H. and Graetsch, H., Chromium incorporation in mullite. *Am. Miner.*, 1990, **75**, 392–397.
25. Fischer, R. X. and Schneider, H., Crystal structure of Cr-mullite. *Am. Miner.*, 2000, **85**, 1175–1179.
26. Schneider, H. and Vasudevan, R., Structural deformation of manganese substituted mullites: X-ray line broadening and lattice parameter studies. *N. Jb. Min. Mh.*, 1989, 165–178.
27. Schneider, H., Solid solubility of Na_2O in mullite. *J. Am. Ceram. Soc.*, 1984, **67**, C130–C131.
28. Schneider, H., Magnesium incorporation in mullite. *N. Jb. Miner. Mh.*, 1985, 491–496.
29. Schneider, H., Zirconium incorporation in mullite. *N. Jb. Miner. Mh.*, 1986, **4**, 172–180.
30. Caballero, A. and Ocana, M., Synthesis and structural characterization by X-ray absorption spectroscopy of tin-doped mullite solid solutions. *J. Am. Ceram. Soc.*, 2002, **85**, 1910–1914.
31. Tomsia, A. P., Saiz, E., Ishibashi, H., Diaz, M., Requena, J. and Moya, J. D. S., Powder processing of mullite/Mo functionally graded materials. *J. Eur. Ceram. Soc.*, 1998, **18**, 1365–1371.
32. Kutty, T. R. N. and Nayak, M., Photoluminescence of Eu^{2+}-doped mullite ($x Al_2O_3 \cdot y \cdot SiO_2$; $x/y = 3/2$ and 2/1) prepared by the hydrothermal method. *Mater. Chem. Phys.*, 2000, **65**, 158–165.
33. Schneider, H., Mechanical properties of mullite. In *Mullite*, ed. H. Schneider and S. Komarneni. Wiley-VCH, Weinheim, 2005, pp. 141–149.
34. Schneider, H., Thermal properties of mullite. In *Mullite*, ed. H. Schneider and S. Komarneni. Wiley-VCH, Weinheim, 2005, pp. 149–164.
35. Vaughan, M. T. and Weidner, D. J., The relationship of elasticity and crystal structure in andalusite and sillimanite. *Phys. Chem. Miner.*, 1978, **3**, 133–144.
36. Young, H., Hazen, R. M., Finger, L. W., Prewitt, C. T. and Downs, R. T., Compressibility and crystal structure of sillimanite, Al_2SiO_5, at high-pressure. *Phys. Chem. Miner.*, 2001, **25**, 39–47.
37. Palko, J. W., Sayir, A., Sinogeikin, S. V., Kriven, W. M. and Bass, J. D., Complete elastic tensor for mullite ($\sim 2.5 Al_2O_3 \cdot SiO_2$) to high temperatures measured from textured fibers. *J. Am. Ceram. Soc.*, 2002, **85**, 2005–2012.
38. Hildmann, B., Ledbetter, H., Kim, S. and Schneider, H., Structural control of elastic constants of mullite in comparison to sillimanite. *J. Am. Ceram. Soc.*, 2001, **84**, 2409–2414.
39. Schreuer, J., Hildmann, B. and Schneider, H., Elastic properties of mullite single crystals up to 1400 °C. *J. Am. Ceram. Soc.*, 2006, **89**, 1624–1631.
40. Touloukian, Y. S. and Buyco, E. H., Heat conductivity—nonmetallic solids. In *Thermo-Physical Properties of Matter*, *Vol 6*. IFI/Plenum, New York, 1970, pp. 254–256.
41. Bass, J. D., Elasticity of minerals, glasses, and melts. In *Mineral Physics and Crystallography—Handbook of Physical Constants*, *Vol 2*, ed. T. J. Ahrens. American Geophysical Union, Washington, 1995, AGU Reference Shelf, pp. 45–63.
42. Hildmann, B. and Schneider, H., Thermal conductivity of 2/1-mullite single crystals. *J. Am. Ceram. Soc.*, 2005, **88**, 2879–2882.
43. Schneider, H. and Eberhard, E., Thermal expansion of mullite. *J. Am. Ceram. Soc.*, 1990, **73**, 2073–2076.
44. Brunauer, G., Boysen, H., Frey, F., Hansen, T. and Kriven, W., High temperature crystal structure of a 3:2 mullite from neutron diffraction data. *Z. Krist.*, 2001, **216**, 284–290.
45. Hartmann, P. and Pedock, W. E., 1955. Cited in Kleber, W., *Einführung in die Kristallographie*. VEB Verlag Technik, Berlin, 1971, pp. 141–142.
46. Schmücker, M., Hildmann, B. and Schneider, H., Mechanism of 2/1- to 3/2-mullite transformation at 1650 °C. *Am. Miner.*, 2002, **87**, 1190–1193.
47. Schmücker, M., Mechnich, P., Zaefferer, S. and Schneider, H., The high-temperature mullite/α-alumina conversion in rapidly flowing water vapor. *Scripta Mater.*, 2006, **55**, 1131–1134.
48. Braue, W., Hildmann, B., Schneider, H., Eldred, B. T. and Ownby, P. D., Reactive wetting of mullite $Al_2[Al_{2+2x}Si_{2-2x}]O_{10-x}$ single crystals by yttrium-aluminosilicate and borosilicate glasses. *J. Mater. Sci.*, 2005, **40**, 2335–2340.
49. Fielitz, P., Bochart, G., Schmücker, M., Schneider, H., Wiedenbeck, M., Rhede, D., Weber, S. and Scherrer, S., Secondary ion mass spectroscopy study of oxygen-18 tracer diffusion in 2/1-mullite single crystals. *J. Am. Ceram. Soc.*, 2001, **84**, 2845–2848.
50. Fielitz, P., Bochart, G., Schneider, H., Schmücker, M., Wiedenbeck, M. and Rhede, D., Self diffusion of oxygen in mullite. *J. Eur. Ceram. Soc.*, 2001, **21**, 2577–2582.
51. Fielitz, P., Bochart, G., Schmücker, M. and Schneider, H., Silicon tracer diffusion in single crystalline 2/1-mullite measured by SIMS depth profiling. *Phys. Chem.*, 2003, **5**, 2279–2282.
52. Fielitz, P., Bochart, G., Schmücker, M. and Schneider, H., Al-26 diffusion measurement in 2/1-mullite by means of secondary ion mass spectroscopy. *Solid State Ionics*, 2006, **177**, 493–496.
53. Hildmann, B. and Schneider, H., Heat capacity of mullite: new data and evidence for a high-temperature phase transformation. *J. Am. Ceram. Soc.*, 2004, **87**, 227–234.
54. Lacks, D., Hildmann, B. and Schneider, H., Effects of disorder in mullite: molecular dynamics simulation abd energy landscape ananlysis. *Phys. Rev. B*, 2005, **72**, 214305-1-5.
55. Schreuer, J., Burianek, M., Mühlberg, M., Winkler, B., Wilson, D. J. and Schneider, H., Crystal growth and elastic properties of orthorhombic $Bi_2Ga_4O_9$. *J. Phys.: Condens. Matter*, 2006, **18**, 10977–10988.